Automated Optical Density Normalization for Myelin Quantification: Cross-Modal Validation with 7T Ex Vivo MRI

Zahra Khodakarami, Sheina Emrani, Pulkit Khandelwal, Chinmayee Athalye, Amanda Denning, Winifred Trotman, Lisa M. Levorse, Eric Teunissen-Bermeo, Hamsanandini Radhakrishnan, Daniel Ohm, Christopher Olm, Noah Capp, Ranjit Ittyerah, Karthik Prabhakaran, John A. Detre, Sandhitsu R. Das, David A. Wolk, Corey T. McMillan, Dylan Tisdall, David J. Irwin, John L. Robinson, Edward B. Lee, Paul A. Yushkevich

University of Pennsylvania, Philadelphia, PA, USA
zkm@seas.upenn.edu

Abstract. White matter hyperintensities (WMH) on T2-weighted MRI are associated with cerebrovascular pathology and neurodegeneration, including myelin loss. Luxol Fast Blue (LFB) histopathology visualizes myelin integrity, and optical density (OD) serves as a quantitative proxy for myelin concentration. However, variability in staining and tissue processing introduces batch effects that confound OD comparison across histology runs. To address this, we present an automated pipeline that identifies reference (non-pathologic) white-matter regions directly from whole-slide images, without manual annotation, and uses them to normalize OD heatmaps. Against expert ratings of myelin-loss severity, automatically selected references matched expert placement ($\rho = 0.88$), and batch-calibrated OD best separated intact tissue from regions of severe myelin loss (AUC = 0.90). In voxel-wise comparison with co-registered 7T ex vivo MRI across 151 sections from 31 hemispheres, batch-calibrated OD correlated best with MRI signal ($\rho = -0.379$), and the correlation persisted within WMH ($\rho = -0.336$), indicating capture of graded myelin loss. By mitigating staining artifacts, this pipeline provides a validated framework for quantitative cross-modal comparison and a foundation for translating histology-derived myelin maps to in vivo imaging biomarkers. Code is available at https://github.com/zkhodakarami/myelin_quantification.

Keywords: Myelin Quantification · WMH · Optical Density

1 Introduction

White matter hyperintensities (WMH), regions of hyperintense signal on T2-weighted (T2w) magnetic resonance imaging (MRI), are prevalent neuroimaging markers of aging associated with stroke, dementia, and cognitive decline [26]. As WMH represent a heterogeneous range of underlying pathologies, including

arteriosclerosis, cerebral amyloid angiopathy, and demyelination, moving beyond volumetric measures to pathologically specific biomarkers is critical [26,8]. However, establishing spatial correspondence between histology and MRI is hindered by the technical variability of histochemical methods. Luxol Fast Blue (LFB) staining is one of the most widely used methods for visualizing myelin sheaths in brain tissue [16,17], providing a clear contrast between grey and white matter structures and making it particularly well-suited for cross-modal alignment with MRI. While semi-quantitative ordinal ratings of myelin "pallor" have been the traditional approach, they are inherently subjective, time-consuming, and too coarse to capture subtle variations in myelin density [6]. Optical density (OD) measurement offers an objective alternative, capturing stain absorption as a continuous proxy for myelin concentration [15,27,10]. However, it remains confounded by variability in tissue preparation and batch effects, which introduce intensity differences across slides unrelated to the underlying biology.

While several computational stain normalization methods, both classical [20,22,25] and deep learning-based [12], exist, they standardize color appearance relative to external reference images to improve the downstream classification tasks. However, these approaches rely on global color statistics without encoding what constitutes biologically intact myelin, and recent studies have shown that substantial inter-batch and inter-laboratory variation persists even after normalization [13,7,18]. **To the best of our knowledge, within histopathology stain normalization, there is no method that normalizes stain absorption to the most intact/stable region of each tissue or batch.**

Without a stable reference baseline, OD values make biological interpretation of stain absorption more challenging and hinder comparison across stained slides. **We reframe stain normalization as a biological reference-discovery problem**: rather than standardizing global color statistics, we automatically identify internal tissue regions where myelin is most likely to be intact and calibrate OD against them, mirroring how neuropathologists implicitly assess myelin loss by judging pallor relative to normal-appearing areas within the same section.

A major rate-limiting and time-consuming step in adjusting for staining variability is the requirement for manual annotations. We address this challenge by leveraging **an inverted-attention mechanism** derived from a CLAM model previously trained to identify histopathological features of cognitive impairment [21]. Specifically, we used the model's ability to detect white matter pallor, a key indicator of myelin loss, to automatically isolate stable reference regions for normalization without manual oversight. By designating areas with the lowest attention scores as candidates for intact myelin, **we effectively converted a pathology-detection network into an annotation-free reference-discovery algorithm**. Combined with blind stain deconvolution, which requires no predefined stain vectors, this approach enables biologically grounded OD calibration that adapts to each slide's specific staining characteristics.

2 Materials and Methods

Dataset. We analyzed 321 LFB–Crystal Violet (CV)-stained whole-slide histology sections from 45 hemispheres (20F/25M, age 76.22 ± 10.05 years, postmortem interval [PMI] 18.76 ± 9.99 hours) spanning the Alzheimer's disease continuum, acquired at the University of Pennsylvania using the 7T ex vivo MRI–guided histology sampling protocol of Athalye et al. [2]. Specimens were obtained with informed consent from next of kin. After formalin fixation, each hemisphere was scanned with a 3D T2 SPACE sequence (0.3 mm^3 isotropic, TR/TE = 3000/383 ms, 2–3 hours per scan). Tissue slabs were then sampled with patient-specific 3D-printed molds, processed into formalin-fixed, paraffin-embedded blocks, sectioned at 20–30 μm, and stained with LFB-CV. Whole-slide images were digitized at 0.4×0.4 μm^2 (20×). For cross-modal evaluation, we used a subset of 151 sections from 31 hemispheres (14F/17M, age 76.81 ± 10.61 years, PMI 17.71 ± 7.48 hours) that passed visual quality control for histology–MRI registration.

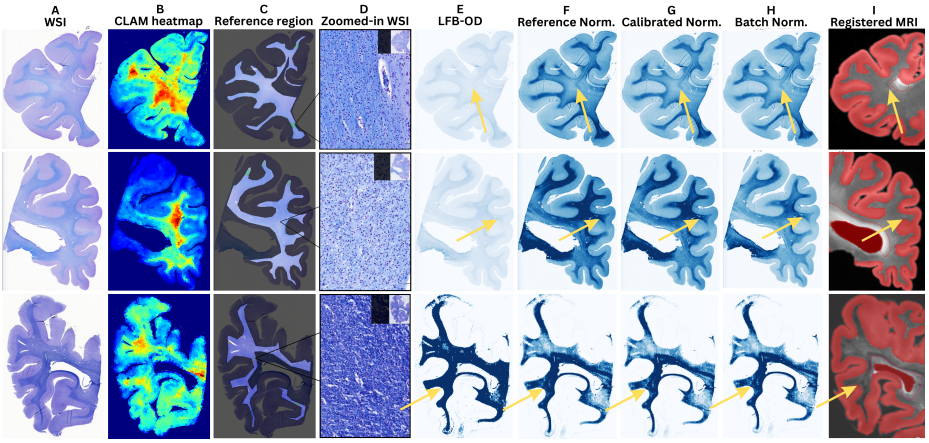

Fig. 1. Proposed pipeline. WSI: whole-slide image; LFB-OD: Luxol Fast Blue optical density; Norm.: normalized; WMH: white-matter hyperintensity. **(A)** Input LFB-CV sections: top two rows, one hemisphere/stain batch; bottom row, a different hemisphere and batch. **(B)** CLAM attention [21] as a superpixel heatmap. **(C)** Reference regions (green): lowest-2% attention superpixels within the white-matter mask. **(D)** Zoomed-in WSI at the location marked in (C). **(E)** OD of the Macenko-deconvolved [20] LFB channel (slides downsampled to 500 px height). **(F–H)** (E) normalized three ways: by each slide's own reference (F), by a calibrated reference OD (G), and by the calibrated most-intact region shared within a batch (H). **(I)** Co-registered ex vivo MRI (non-WM masked red; WMH outlined) for cross-modal evaluation. Arrows indicate corresponding regions across (E)–(I). Details in Secs. 2.1 and 2.2.

Our method takes as input LFB-CV-stained whole-slide images of brain tissue and produces normalized optical density (OD) maps of myelin content. Then

they are used for cross-modal comparison with registered T2w MRI to compare gold-standard myelin loss heatmaps with WMH on MRI. As illustrated in Fig. 1, the pipeline proceeds as follows: given a set of WSI (A), superpixel-level attention heatmaps using the CLAM model were generated (B). The lowest-attention superpixels within the white matter were selected as candidate reference regions (C). Following stain deconvolution to separate LFB and CV channels, OD heatmaps for the LFB channel were generated (E). OD heatmaps were then normalized against the reference region OD values using three strategies of increasing robustness: per-slide, calibrated, and batch-calibrated normalization(F–H). Finally, registered ex vivo T2w MRIs to the histology coordinate spaces were used to evaluate spatial correspondence between normalized myelin-density heatmaps and MRI signal intensity within white matter and WMH regions (I). While the current paper focuses on comparing LFB-derived OD measures to ex vivo MRI, future work will incorporate in vivo FLAIR MRI, which is available in most cases at the center.

2.1 WSI Processing

White Matter Segmentation. White matter masks were obtained automatically with nnU-Net v2 [11], a widely adopted and well-validated default for biomedical image segmentation [11,9]. The model, trained on 256 manually segmented WSIs (mean Dice 0.896 on 65 held-out images), was applied to WSIs downsampled to a fixed height of 500px. Manual annotations excluded regions that neuropathologists ignore when identifying intact myelin: cut edges (darker LFB from sectioning artifacts) and periventricular tracts (disproportionately high OD from dense fiber packing, not representative of typical white matter). The inverted-attention reference-discovery step is agnostic to this backbone; any white matter mask of comparable quality can be substituted.

Stain Deconvolution and Optical Density. Per-slide blind color deconvolution isolates the LFB channel from the CV counterstain [20,23]. Background illumination I_0 is estimated from the 99th percentile of pixel intensities, and OD is computed via the Beer–Lambert transform: $\mathrm{OD} = -\log_{10}(I/I_0)$. Tissue pixels are identified as those with $\max_c(\mathrm{OD}_c) \geq 0.05$ and $\sum_c \mathrm{OD}_c \leq 3.0$, where c indexes the RGB channels. Stain vectors are resolved via SVD of the tissue OD matrix, followed by angular peak detection in the two-dimensional projection plane, adapted from QuPath's [3] blind source separation, requiring no predefined reference vectors. The OD matrix is then projected onto the estimated LFB stain vector to obtain per-pixel LFB optical density, which is retained for all downstream analyses.

Attention-Based Reference Region Selection. CLAM is a weakly supervised, attention-based classifier for whole-slide images: by predicting a slide-level label, it assigns each tissue region an attention score that quantifies how much that region drives the prediction [19]. We repurpose the pretrained CLAM model of McKenzie et al. [21], which was trained to distinguish cognitively impaired from unimpaired donors using hippocampal and frontal cortex tissue, regions highly susceptible to age-related myelin breakdown [4,5,10]. Because myelin

pallor is a dominant discriminative feature, the network assigns high attention to white matter with reduced LFB staining. The softmax normalization enforces a complementary constraint: attention on pathology is withdrawn from intact tissue. We exploit this inverse relationship to select reference white matter for OD normalization, hypothesizing that the lowest-attention regions correspond to intact myelin across diagnostic groups.

Each WSI is tiled at 20× (256×256 px, center-cropped to 224×224) for ResNet-50 feature extraction. Patch-level attention scores are softmax-normalized, back-projected to a tile-grid heatmap, and Gaussian-smoothed ($\sigma = 1.5$ tiles). The WSI is independently partitioned into SLIC superpixels [1] in CIELAB space (n=2000, compactness=10, σ=1.0), restricted to those with at least 50% white matter overlap (S_{WM}). Each superpixel's score $\bar{A}(s)$ is the area-weighted mean of underlying heatmap values. We select as the reference region $S_{\mathrm{ref}} = \{s \in S_{\mathrm{WM}} : \bar{A}(s) \leq \tau_{0.02}\}$, where $\tau_{0.02}$ is the 2^{nd} percentile of attention within S_{WM}, we define the per-slide reference OD as the mean LFB optical density across S_{ref}. Although the CLAM model was trained on a different cohort and scanner, the shared LFB chromogen preserves the relevant feature space; we validated that CLAM-identified references concord with expert-placed intact regions.

Normalization Strategies. We evaluate four strategies in a consistent progression. Let $\mathrm{OD}_{\mathrm{ref}}$ denote the per-slide CLAM-derived reference and $\mathrm{OD}_{\max}(b)$ the maximum calibrated reference across all slides in batch b (same subject and staining session). Raw OD is used as-is; internal-normalized divides by $\mathrm{OD}_{\mathrm{ref}}$; calibrated divides by $1.1 \times \mathrm{OD}_{\mathrm{ref}}$, where the slope correction derives from the CLAM-vs-expert linear fit (Section 3); and batch-normalized divides by $\mathrm{OD}_{\max}(b)$. All normalized values are capped at 1.5, beyond which transmittance falls below 3% of incident light ($10^{-1.5}$), exceeding both the reliable dynamic range of brightfield scanning and the optical density of the most densely myelinated white matter in our dataset.

2.2 MRI-to-Histology Registration

Histology was sampled using an ex vivo 7T T2w MRI-guided protocol [2], and the MRI was registered to the histology using greedy diffeomorphic registration [28] with histology as the fixed target. Segmentation of the T2w MRI was performed using the purple-mri pipeline [14]. N4 bias field correction [24] was applied to the hemisphere MRI to correct for spatial intensity inhomogeneity, using a binary mask derived from the hemisphere segmentation to restrict correction to intracranial tissue. T2w intensities were then z-score normalized using the corpus callosum (CC) as an internal reference, selected because it is the most densely myelinated white matter structure, yielding consistently low T2w signal across subjects. On this normalized scale, values near zero correspond to intact myelin, while increasingly positive values indicate progressively abnormal tissue. The normalized MRI, along with white matter masks restricted to normal appearing white matter, WMH, and CC, were warped to histology space via nearest-neighbor interpolation for cross-modality evaluation.

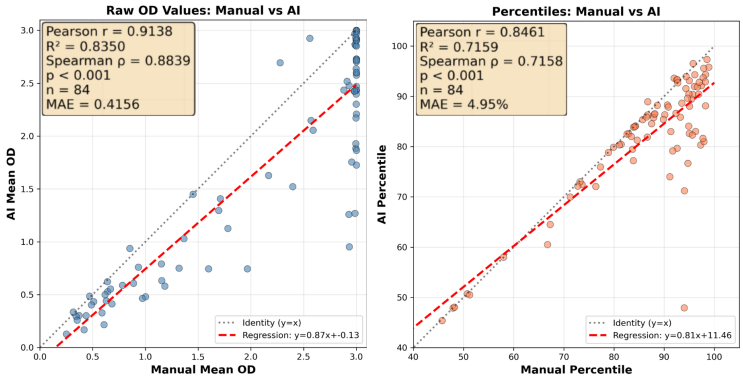

Fig. 2. Validation of CLAM-based reference region selection against manual expert placement across 84 slides. Left: raw Luxol Fast Blue Optical Density(LFB-OD) values (Pearson $r = 0.91$). Right: percentile-transformed values (Pearson $r = 0.85$).

3 Experiments and Results

3.1 WSI Evaluation Results

To validate CLAM-based reference selection, we compared mean OD of CLAM-identified regions against manually identified intact regions across 84 slides. Two trained raters independently placed reference regions on each slide; discrepant placements were reviewed jointly and resolved by consensus. The consensus reference OD showed strong agreement with CLAM-derived reference OD (Pearson $r = 0.91$, Spearman $\rho = 0.88$, $p < 0.001$). The regression slope of 0.87 motivated the $\beta = 1.15$ calibration correction in the calibrated normalization strategy (Fig. 2).

3.2 Expert Pathology Grading

We assessed four OD quantification strategies against expert pathology ratings across 97 ROIs rated on the 0–3 myelin loss scale of Deramecourt et al. [6]. Two trained raters independently rated each ROI; discrepant scores were reviewed jointly and resolved by consensus. Batch-normalized OD achieved the strongest correlation with consensus grades ($\rho = -0.64$, $p < 0.001$), followed by raw ($\rho = -0.52$), calibrated ($\rho = -0.49$), and internal-normalized OD ($\rho = -0.46$). Batch normalization also yielded the highest discrimination between intact (grade 0) and severe myelin-loss (grades 2–3) tissue (AUC = 0.90), compared with raw (AUC = 0.85), calibrated (AUC = 0.82), and internal-normalized (AUC = 0.81). Raw OD exhibited extreme technical variability among grade-0 (intact) regions (CV = 178.6%), driven in part by non-physical values arising from tissue folds and deconvolution artifacts. Even after truncation at OD = 1.5, raw CV remained high (49.4%), whereas internal normalization

reduced it to 9.6%, demonstrating that reference-based normalization addresses both artifactual outliers and genuine staining heterogeneity(Fig. 3).

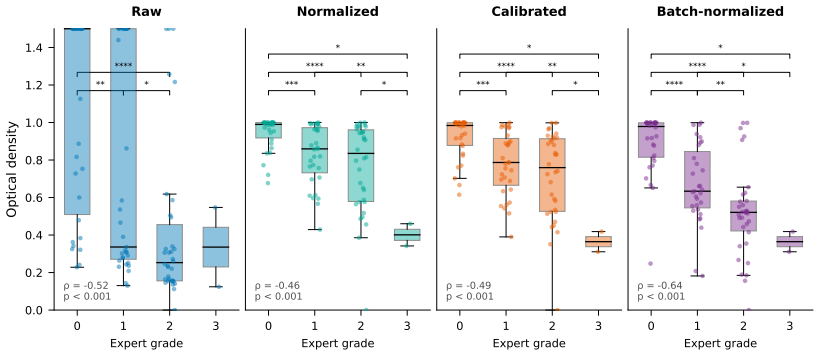

Fig. 3. Distribution of Luxol Fast Blue Optical Density by expert pathology grade (0 = intact, 3 = severe myelin loss; $n = 97$ ROIs) across four quantification methods. More details in section 3.2. Statistical comparisons: $*p < 0.05$, $**$ $p < 0.01$, $***p < 0.001$, $****$ $p < 0.0001$.

3.3 Cross-Modal Evaluation Results

We evaluated voxel-wise correspondence between LFB OD and T2w MRI across 151 co-registered sections from 31 hemispheres within full white matter and WMH masks. Given the CC z-score normalization, the expected relationship is negative: high OD reflects intact myelin (near-zero z-score), whereas demyelination yields reduced OD and elevated T2w signal. Table 1 summarizes all metrics.

Batch normalization achieved the strongest voxel-wise Spearman correlation ($\rho = -0.379 \pm 0.204$), significantly outperforming raw OD, internal, and calibrated normalization across all metrics. Given the inherent limitations of cross-modal histology–MRI comparison, including microscopic registration errors and resolution mismatch, these correlations represent robust correspondence [2]. Shift analysis confirmed impact of residual registration error (best ρ within ± 3 pixels improved from -0.379 to -0.424). Moreover, spatial overlap was assessed by independently thresholding each modality (bottom 25th percentile OD; top 75th percentile T2w) and computing Dice and AUC-ROC between the resulting lesion maps. To account for non-independence of multiple sections per hemisphere (4.9 ± 3.3), paired t-tests on hemisphere-level means confirmed all normalization methods significantly outperformed raw OD (all $p < 10^{-5}$), with batch normalization significantly exceeding internal ($p = 1.0 \times 10^{-4}$) and calibrated ($p = 6.8 \times 10^{-3}$) normalization. Within WMH regions, the correlation persisted ($\rho = -0.336 \pm 0.303$), confirming that cross-modal agreement reflects a continuous relationship within affected white matter.

Table 1. Cross-modal evaluation of Luxol Fast Blue Optical Density against T2w ex vivo MRI across 151 histology sections. **Values are reported as $\times 10^{-2}$ (mean $\pm$ SD)**. Across all normalized methods, 148 of 151 sections (98%) achieved significant voxel-wise correlation ($p < 0.05$) within white matter, and 108 of 125 sections (86%) within WMH regions. Best shift ρ: best Spearman correlation achievable within a $\pm$3-pixel spatial shift, quantifying sensitivity to residual registration error. Best values per metric in **bold**.

Metric	Raw	Internal-norm.	Calibrated	Batch-norm.
All white matter (n = 151)				
Spearman ρ	-23.8 ± 22.7	-35.6 ± 19.8	-36.6 ± 20.0	$\mathbf{-37.9 \pm 20.4}$
Best shift ρ	-27.9 ± 26.1	-40.3 ± 22.1	-41.3 ± 22.3	$\mathbf{-42.4 \pm 23.1}$
Pearson r	-19.6 ± 21.1	-31.0 ± 19.6	-32.6 ± 20.0	$\mathbf{-33.5 \pm 19.7}$
Dice coefficient	32.9 ± 17.6	42.6 ± 14.0	42.8 ± 14.1	$\mathbf{43.2 \pm 14.0}$
Area under ROC	62.0 ± 12.1	68.8 ± 11.3	69.3 ± 11.5	$\mathbf{69.8 \pm 11.6}$
WMH only (n = 125)				
Spearman ρ	-23.0 ± 28.1	-32.8 ± 29.8	-33.1 ± 29.9	$\mathbf{-33.6 \pm 30.3}$
Pearson r	-22.8 ± 26.8	-33.0 ± 28.4	-33.4 ± 28.3	$\mathbf{-33.4 \pm 28.2}$

4 Discussion

LFB staining intensity varies substantially across slides due to fixation, section thickness, and staining protocol differences, producing a continuous OD gradient whose absolute values are not directly comparable across sections. Our attention-based approach addresses this by automatically identifying intact white matter as an internal reference ($r = 0.91$ with expert selection). Per-slide internal normalization minimizes within-slide variability, reducing the coefficient of variation within intact regions from 178.6% to 9.6%; batch normalization trades a modestly higher CV (18.5%) for cross-session comparability, which underlies its stronger agreement with expert grades and MRI. Furthermore, the pipeline is robust to domain shifts in tissue origin and scanner type. Because the shared LFB chromogen preserves the underlying feature space of myelin pallor, the repurposed CLAM model generalizes well beyond its original training data in the hippocampus and frontal cortex.

To our knowledge, the cross-modal validation against the co-registered 7T MRI across 151 sections from 31 hemispheres represents the largest voxel-wise histology–MRI correlation study of myelin integrity at this resolution. The observed correlations ($\rho = -0.379$) are notable given inherent cross-modal limitations: registration errors, resolution mismatch, and the distinct physical bases of LFB OD and T2 relaxation. Indeed, as demonstrated by our spatial shift analysis, even microscopic misalignments severely artificially suppress the theoretical maximum correlation. That the correlation persists within WMH regions ($\rho = -0.336$) confirms the pipeline captures a continuous spectrum of myelin pathology, not merely lesional versus non-lesional contrast. This quantitative link between histological myelin density and MRI signal opens a concrete downstream application: using the histology-derived OD maps of myelin as voxel-level

ground truth to train or calibrate models that predict regional myelin loss from in vivo FLAIR MRI.

Several limitations should be noted. Analyses were conducted with a single MRI protocol; generalizability to other sequences remains to be established. Batch normalization requires multiple slides from the same staining session, though internal normalization provides a practical single-slide alternative.

Conclusion. We presented a novel reference-discovery algorithm that leverages an inverted-attention mechanism and blind stain deconvolution for automated, quantitative myelin assessment in LFB-CV histology. Validated against expert ordinal ratings and through the largest voxel-wise histology-MRI correlation study of its kind (151 co-registered 7T MRI and histology sections), our results demonstrate that batch-calibrated normalization yields the most consistent and biologically grounded measure of myelin integrity. By successfully mitigating staining variability, this pipeline captures myelin loss and establishes a robust histochemical foundation for the development and calibration of in vivo imaging biomarkers.

Acknowledgments. This work was supported by NIH grants R01 AG056014, P30 AG072979 and R01 AG069474.

Disclosure of Interests. The authors have no competing interests to declare that are relevant to the content of this article.

References

1. Achanta, R., et al.: SLIC Superpixels Compared to State-of-the-Art Superpixel Methods. IEEE Transactions on Pattern Analysis and Machine Intelligence **34**(11), 2274–2282 (Nov 2012). https://doi.org/10.1109/TPAMI.2012.120
2. Athalye, C., et al.: Operationalizing postmortem pathology-MRI association studies in Alzheimer's disease and related disorders with MRI-guided histology sampling. Acta Neuropathologica Communications **13**(1), 120 (May 2025). https://doi.org/10.1186/s40478-025-02030-y
3. Bankhead, P., et al.: QuPath: Open source software for digital pathology image analysis. Scientific Reports **7**(1), 16878 (Dec 2017). https://doi.org/10.1038/s41598-017-17204-5
4. Bartzokis, G.: Age-related myelin breakdown: a developmental model of cognitive decline and Alzheimer's disease. Neurobiology of Aging **25**(1), 5–18 (Jan 2004). https://doi.org/10.1016/j.neurobiolaging.2003.03.001
5. Bartzokis, G., Lu, P.H., Mintz, J.: Human brain myelination and amyloid beta deposition in Alzheimer's disease. Alzheimer's & Dementia **3**(2), 122–125 (Apr 2007). https://doi.org/10.1016/j.jalz.2007.01.019
6. Deramecourt, V., et al.: Staging and natural history of cerebrovascular pathology in dementia. Neurology **78**(14), 1043–1050 (Apr 2012). https://doi.org/10.1212/WNL.0b013e31824e8e7f
7. Dunn, C., et al.: An international study of stain variability in histopathology using qualitative and quantitative analysis. Journal of Pathology Informatics **17**, 100423 (Apr 2025). https://doi.org/10.1016/j.jpi.2025.100423

8. Gouw, A.A., et al.: Heterogeneity of small vessel disease: a systematic review of MRI and histopathology correlations. Journal of Neurology, Neurosurgery & Psychiatry **82**(2), 126–135 (Feb 2011). https://doi.org/10.1136/jnnp.2009.204685
9. Helgesen, S.E.M., et al.: Reliable and efficient tissue segmentation in whole-slide images. In: MICCAI Workshop on Computational Pathology with Multimodal Data (COMPAYL) (2025)
10. Ihara, M., et al.: Quantification of myelin loss in frontal lobe white matter in vascular dementia, Alzheimer's disease, and dementia with Lewy bodies. Acta Neuropathologica **119**(5), 579–589 (May 2010). https://doi.org/10.1007/s00401-009-0635-8
11. Isensee, F., et al.: nnU-Net: a self-configuring method for deep learning-based biomedical image segmentation. Nature Methods **18**(2), 203–211 (Feb 2021). https://doi.org/10.1038/s41592-020-01008-z
12. Kang, H., et al.: StainNet: A Fast and Robust Stain Normalization Network. Frontiers in Medicine **8**, 746307 (Nov 2021). https://doi.org/10.3389/fmed.2021.746307
13. Khan, U., et al.: Staining normalization in histopathology: Method benchmarking using multicenter dataset (2025). https://doi.org/10.48550/ARXIV.2506.19106, version Number: 1
14. Khandelwal, P., et al.: Automated deep learning segmentation of high-resolution 7 Tesla postmortem MRI for quantitative analysis of structure-pathology correlations in neurodegenerative diseases. Imaging Neuroscience **2**, imag–2–00171 (May 2024). https://doi.org/10.1162/imag_a_00171
15. Khodanovich, M.Y., et al.: Histological validation of fast macromolecular proton fraction mapping as a quantitative myelin imaging method in the cuprizone demyelination model. Scientific Reports **7**(1), 46686 (Apr 2017). https://doi.org/10.1038/srep46686
16. Kiernan, J.A.: Histological and Histochemical Methods: Theory and Practice. Scion Publishing, Banbury, UK, 5th edn. (2015)
17. Klüver, H., Barrera, E.: A Method for the Combined Staining of Cells and Fibers in the Nervous System. Journal of Neuropathology & Experimental Neurology **12**(4), 400–403 (Oct 1953). https://doi.org/10.1097/00005072-195312040-00008
18. Lin, S., et al.: Impact of stain variation and color normalization for prognostic predictions in pathology. Scientific Reports **15**(1), 2369 (Jan 2025). https://doi.org/10.1038/s41598-024-83267-w
19. Lu, M.Y., et al.: Data-efficient and weakly supervised computational pathology on whole-slide images. Nature Biomedical Engineering **5**(6), 555–570 (Mar 2021). https://doi.org/10.1038/s41551-020-00682-w
20. Macenko, M., et al.: A method for normalizing histology slides for quantitative analysis. In: 2009 IEEE International Symposium on Biomedical Imaging: From Nano to Macro. pp. 1107–1110. IEEE, Boston, MA, USA (Jun 2009). https://doi.org/10.1109/ISBI.2009.5193250
21. McKenzie, A.T., et al.: Interpretable deep learning of myelin histopathology in age-related cognitive impairment. Acta Neuropathologica Communications **10**(1), 131 (Sep 2022). https://doi.org/10.1186/s40478-022-01425-5
22. Reinhard, E., et al.: Color transfer between images. IEEE Computer Graphics and Applications **21**(4), 34–41 (Aug 2001). https://doi.org/10.1109/38.946629
23. Ruifrok, A.C., Johnston, D.A.: Quantification of histochemical staining by color deconvolution. Analytical and Quantitative Cytology and Histology **23**(4), 291–299 (2001)

24. Tustison, N.J., et al.: N4ITK: Improved N3 Bias Correction. IEEE Transactions on Medical Imaging **29**(6), 1310–1320 (Jun 2010). https://doi.org/10.1109/TMI.2010.2046908
25. Vahadane, A., et al.: Structure-Preserving Color Normalization and Sparse Stain Separation for Histological Images. IEEE Transactions on Medical Imaging **35**(8), 1962–1971 (Aug 2016). https://doi.org/10.1109/TMI.2016.2529665
26. Wardlaw, J.M., et al.: What are White Matter Hyperintensities Made of?: Relevance to Vascular Cognitive Impairment. Journal of the American Heart Association **4**(6), e001140 (Jun 2015). https://doi.org/10.1161/JAHA.114.001140
27. Warntjes, J., et al.: Myelin Detection Using Rapid Quantitative MR Imaging Correlated to Macroscopically Registered Luxol Fast Blue–Stained Brain Specimens. American Journal of Neuroradiology **38**(6), 1096–1102 (Jun 2017). https://doi.org/10.3174/ajnr.A5168
28. Yushkevich, P.A., et al.: IC-P-174: Fast Automatic Segmentation of Hippocampal Subfields and Medial Temporal Lobe Subregions In 3 Tesla and 7 Tesla T2-Weighted MRI. Alzheimer's & Dementia **12**(7S_Part_2) (Jul 2016). https://doi.org/10.1016/j.jalz.2016.06.205